A low-profile wall shear comparator to mount and test surface samples

Muchen Xu[1,†,‡], Blaine Arihara[1], Hao Tong[1,+], Ning Yu[1], Yuta Ujiie[1,^], Chang-Jin "CJ" Kim[1,2,3,*]

[1]Mechanical and Aerospace Engineering Department, University of California, Los Angeles (UCLA), Los Angeles, CA 90095, USA.
[2]Bioengineering Department, University of California, Los Angeles (UCLA), Los Angeles, CA 90095, USA.
[3]California NanoSystems Institute (CNSI), University of California, Los Angeles (UCLA), Los Angeles, CA 90095, USA.

Abstract

Accurate measurement of shear stress on a solid surface is a crucial but challenging task in fluid mechanics. Different sensors are usually used for different experimental settings: water channel, wind tunnel, towing tank, watercraft, aircraft, etc. This paper presents a direct shear sensor designed to work for varying test objects and flow conditions. Designed to compare two different sample surfaces, the shear sensor is comprised of two floating elements, whose displacement is proportional to the shear stress they experience, and two optical encoders, which measure the displacements precisely, right under the floating elements. The main plate includes two identical sets of floating elements and flexure beams machined monolithically from a thick piece of metal, allowing displacements in only one in-plane direction. The side-by-side arrangement allows the two floating elements to experience essentially the same flow conditions, regardless of test condition, enabling the comparative sensing. The method of machining these folded-beam flexures, whose width is on the scale of micrometers, while thickness and length are in millimeters and centimeters, respectively, is presented. The main plate is designed with the help of finite element analysis to ensure dynamic response of the floating elements is appropriate for target flow conditions. The utility of the shear sensor is verified in three different flow settings, i.e., water tunnel, boat in open water, and wind tunnel. A miniature underwater camera system is also developed to observe the sample surfaces during testing on a moving object, such as a boat.

1 Background and introduction

The shear stress of a fluid flow on a solid surface is a critical piece of information in fluid mechanics and measured by indirect or direct methods. For direct measurements, conventionally a floating element is mounted on a balance, and the shear force exerted on the floating element is obtained by measuring its resulting displacement or reading the force required to keep it in its original position (Winter 1979; Haritonidis 1989). Typically, a single pivot is used as the balance, and the displacement is measured by a strain gauge (Schetz 2010; Bidkar et al. 2014; Meritt and Schetz 2014). However, the commonly used piezoresistive gauge is sensitive to temperature and fluid pressure changes, requiring calibration prior to each test (Bidkar et al. 2014). Since the pivot is perpendicular to the shear plane, the single pivot sensors are usually thick (tall) compared to other in-plane sensors, which employ beams deflecting in the same plane as the shear plane. This increased thickness (height) is problematic for applications that require a low profile (e.g., airplane wing, ship hull). Furthermore, once assembled, the sensors take on a three-dimensional structure, increasing the cost and complexity of the system when compared with in-plane sensors.

More recently, micro electro mechanical system (MEMS)-based sensors have shown advantages of monolithic structure, compactness, high sensitivity and accuracy, and often high spatial and temporal resolution to support active flow control (Ho and Tai 1998; Chandrasekharan et al. 2011; Natarajan et al. 2014; Shajii et al. 1992; Sheplak et al. 2004; Zhang et al. 2012). However, MEMS sensors are generally too brittle or fragile for repeated sample attachment or use under violent flow conditions. They are also limited to a few centimeters in size due to the size of wafers used in their fabrication, making it difficult to measure average shear stress over large areas. With advances in different functional surfaces (e.g., drag-reducing, antifouling), there is an increasing need for measuring flow shear stress on customized surfaces under varied flows in environment conditions (Aljallis et al. 2013; Bidkar et al. 2014; Sun et al. 2015; Xu 2017). A reliable shear sensor that can mount different surface

† Email address for correspondence: morleyxjtu@ucla.edu
‡ Current affiliation: ASML US, San Diego, USA
+ Current affiliation: Tsinghua University, Beijing, China
^ Current affiliation: Nagoya University, Nagoya, Japan
* Email address for correspondence: cjkim@ucla.edu

samples and work in a variety of liquid and air flows is desired.

One motivation for developing a reliable shear sensor in this report is to measure the drag reduction of superhydrophobic (SHPo) surfaces. With their ability to trap air within their surface microstructures, SHPo surfaces have shown great promise for drag reduction by creating an effective slip in water (Choi and Kim 2006; Rothstein 2010). In laminar flows, SHPo drag reduction is now well understood (Lee et al. 2016), and giant slips, defined to be over 100 μm, have been obtained (Lee et al. 2008; Jung and Bhushan 2010; Lee et al. 2016). However, in turbulent flows, which represent most real-world applications, SHPo drag reduction is still controversial, with inconsistent experimental results. Additionally, drag reduction has never been obtained on marine vessels in open water, even after decades of research. Random-roughness SHPo surfaces were spray-coated on a macroscale (~1 m) object and tested in a towing tank, but the friction drag was found to increase rather than decrease at high Reynolds numbers (Aljallis et al. 2013). On the other hand, parallel grating SHPo surfaces, while most promising based on numerical studies and small-scale experiments, are yet to be made large enough to cover a macroscale object needed for high Reynolds flows in open water. The lack of reliable shear sensors to measure the friction drag of small (e.g., centimeters) sample surfaces in open water turbulent flows have significantly hampered SHPo surface development.

In this paper, we report the development of a novel shear stress sensor for direct measurement of flow shear stress. The shear sensor is conceived to mount a pair of customized surface samples of varying sizes and accurately measure the relative shear forces between them in fluid flows even under environmental fluctuations. The entire sensor system is low-profile and can be incorporated into existing flow facilities or marine vessels. This paper first discusses the sensing principles and design of the sensor system. Then it details the machining process to fabricate floating elements suspended by extremely flexible yet robust beam springs monolithically out of a single piece of metal. After characterizing the sensor system, its performance is demonstrated in various flow facilities, including a water tunnel, wind tunnel, and on a boat in open water. Furthermore, considering the importance of the plastron on SHPo surfaces under water, a miniature underwater camera system is developed to allow users to visually observe and record the sample surface located on the shear sensor during flow experiments.

2 Sensor principles and design

2.1 Sensing principle

As a direct shear sensor, the shear force exerted by the flow over a floating element directly displaces the floating element, which is suspended by a set of flexure beams. The displacement is linear with respect to the shear force and is precisely measured using an optical encoder. As illustrated in Fig. 1, the shear sensor has two floating elements, each suspended by an identical set of beam springs (Fig. 1a) and measured independently by their own encoder (Fig. 1b). As shown in the top view of Fig. 1a, the two floating elements are monolithically formed out of a metal plate (main plate in Fig. 1) using wire electric discharge machining (wire-EDM). Fig. 1b shows the cross-sectional view of a sample surface of interest (e.g., SHPo surface) attached onto the floating element using screws inserted from the bottom of the floating element. A cover plate is used to ensure the sample surfaces are flush with the rest of the sensor surface, which is critical for minimizing measurement error (Haritonidis 1989; MacLean and Schetz 2003). Additionally, in-plane gaps are left between the sample surfaces and the cover plate to accommodate the displacement of the floating elements caused by fluid flow. These gaps are minimized using a feeler gauge because large gaps disturb the fluid flow (MacLean and Schetz 2003). An optical encoder (M2000 linear encoder, Celera Motion Inc.) is used to measure the displacement of each floating element. As shown in the cross-section view of Fig. 1b, the optical encoder measures the displacement of an optical scale attached onto the back of the floating element. The encoder is encapsulated inside of the waterproof encoder plate. During operation, the optical encoder emits a laser beam onto the scale and detects the change in diffraction patterns from the reflected light, allowing it to measure displacements with a spatial resolution of 78 nm. Although the current design is intended to obtain relative shears between two surfaces in real time, if desired, the shear force on each surface can also be calculated in real-time by multiplying the displacement reading of the encoder with the spring constant of the beams obtained from a post-machining calibration described later.

One challenge for direct shear-stress sensors is that they must be highly sensitive to wall shear stress forces in the flow direction and insensitive to forces in all other directions, especially in the direction of wall pressure because the pressure fluctuations in a turbulent boundary layer can be an order of magnitude higher than the corresponding streamwise shear stress (Chandrasekharan et al. 2011; Zhang et al. 2008). To achieve this goal, the flexure beams are designed such that the thickness (into the paper) and length of the

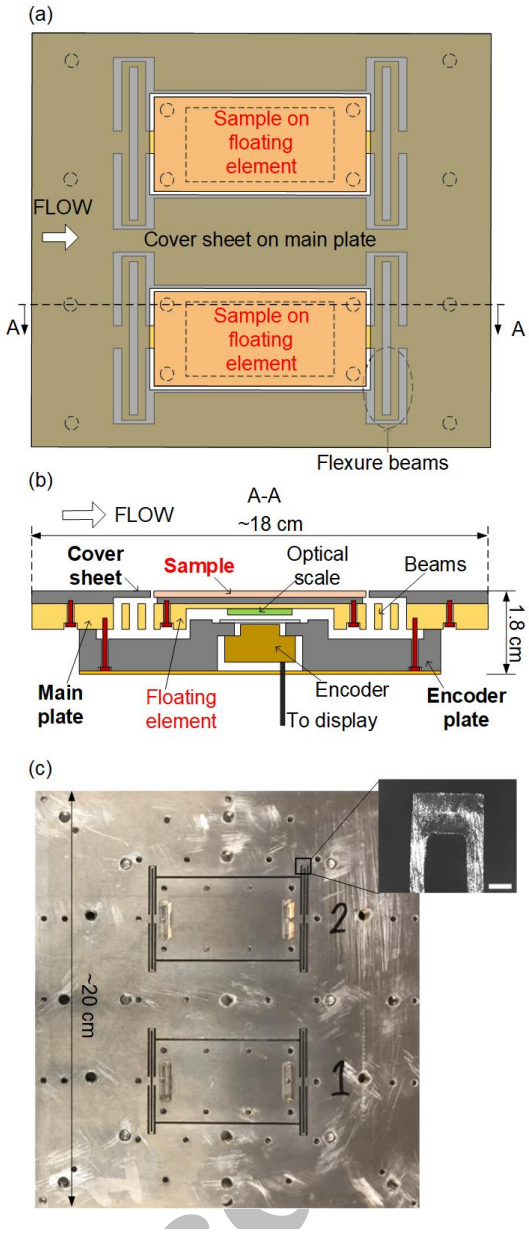

Fig. 1 The shear sensor with two floating elements for direct shear measurements and comparison. **a** Schematic top view of the shear sensor, showing two floating elements (with sample surfaces on them) each suspended from the main plate by a set of flexure beams. The cover sheet on the main plate is drawn with a semi-transparent color to show the flexure beams underneath. Note the gaps between the sample surfaces and the cover sheet are drawn exaggerated to be seen. **b** Schematic cross-section view of the shear sensor, which is a mechanical assembly of the main plate and the encoder plate. **c** Optical picture of the main plate with a zoomed-in picture of the beam at the folded region. The white scale bar in the zoomed-in picture is 500 μm.

beams are much greater (millimeters and centimeters, respectively) than the streamwise width (micrometers) of the beams. These high aspect ratios ensure the spring constant in both the spanwise (traverse to flow) and vertical-to-shear-plane (vertical from the wall) directions are much larger than that of the flow direction. This extreme beam profile cannot be obtained with MEMS fabrication techniques as the beam thicknesses are usually restricted by the silicon wafer thickness and etching depth (< 1 mm), but has been achieved in this paper from a thick (~6 mm) metal plate by developing a special wire-EDM process.

2.2 Floating element structural design

In designing the structural dimensions of the floating elements and flexure beams, the following items were considered: flow conditions, encoder resolution, manufacturing limitations and resonance frequency. The first step was to determine the spring constant, which should be designed to ensure that (1) the actual displacement is much larger than the encoder resolution so that high precision measurement can be achieved and (2) the displacement should be only a few wall units so that the disturbance to the flow created by gaps between the floating element and the surrounding cover sheet (Naughton and Sheplak 2002; MacLean and Schetz 2003) can be ignored. For example, for turbulent boundary layer flow at Reynolds number Re_x ranging from 1×10^6 to 5×10^6, which is a typical Reynolds number range for a small boat, the shear stress τ is estimated to be between 2 and 36 Pa. Making an assumption that the sample size is 5 cm x 5 cm, the shear force applied on the floating element is between 5 and 90 mN. Accordingly, the spring constant is designed to be ~8000 N/m so that the displacement of the floating element is roughly 1 to 10 μm. With an encoder resolution of 78 nm, the minimum displacement is more than 10 times that of the encoder resolution—a high factor of safety. Meanwhile, the wall unit for the above Reynolds number range is roughly 0.5 to 5 μm, so the displacement is only several wall units, ensuring minimal error.

With the spring constant determined as above, the detailed beam dimensions can be designed using classic Euler-Bernoulli beam theory. For folded flexure beams shown in Fig. 1a, the relationship between spring constant and beam dimension is:

$$k = \frac{24EI}{l^3} = 2Et\left(\frac{w}{l}\right)^3 \qquad (1)$$

where l is total beam length, w is beam width, t is beam thickness (i.e., plate thickness), E is Young's modulus, and I is moment of inertia for bending in the flow direction of the beam cross section. The minimum

width of the beam is limited by wire-EDM capability to be 0.25 to 0.5 mm. To obtain ~8000 N/m of spring constant, the beam is designed to be made from a 5 to 6 mm thick plate and is 50 to 80 mm long. Using the above dimensions, a high width-to-thickness ratio ensures the floating element is flexible only in the streamwise direction and much stiffer (by several orders of magnitude) in all other directions.

The dynamic characteristics of the floating element have also been considered during the design process to avoid sensor resonance. Fig. 2a shows the vibration model, where m_0 is the floating element mass, k is the spring constant of the set of flexure beams that suspend the floating element, c is the damping coefficient of the floating element when moving, $x(t)$ is the relative distance between the floating element and the sensor substrate, and the vibration input $d(t)$ is the displacement of the sensor substrate with respect to the inertial reference frame. For example, the displacement of the sensor substrate $d(t)$ may be caused by the water tunnel wall where the shear sensor (including the encoder) is attached because a water pump vibrates the water tunnel. The relative distance $x(t)$ is what the encoder reads, while the substrate movement $d(t)$ is usually unavailable. The equation of motion of the floating element, after applying a Laplace transformation, is:

$$(ms^2 + cs + k)X(s) + ms^2 D(s) = 0 \quad (2)$$

The transfer function between the vibration input and sensor output is:

$$TR = \left|\frac{X(s)}{D(s)}\right| = \frac{\beta^2}{\sqrt{(1-\beta)^2 + (2\xi\beta)^2}} \quad (3)$$

where natural frequency is $\omega_n = \sqrt{k/m}$, damping ratio is $\xi = c/(2m\omega_n)$ and $\beta = \omega/\omega_n$. Fig. 2b plots the transfer function at different damping ratios. As shown in Fig. 2b, the floating element behaves as a "high-pass filter", filtering out (i.e., insensitive to) vibration frequencies that are lower than the resonant frequency. The common environmental noise at different flow facilities was observed to be less than 60 Hz, so the resonant frequency of the floating element was maximized by minimizing its mass, which was achieved by creating a recess in the backside of the floating element, as shown in Fig. 1b. For the shear sensor tested in this report, the resonance frequency was designed to be ~120 Hz.

2.3 Floating element finite element analysis

Finite element analysis (FEA) was used to verify mechanical characteristics of the floating element, including spring constant, resonant frequency and associated resonant modes. Three-dimensional (3D) models of the floating element and beams with precise

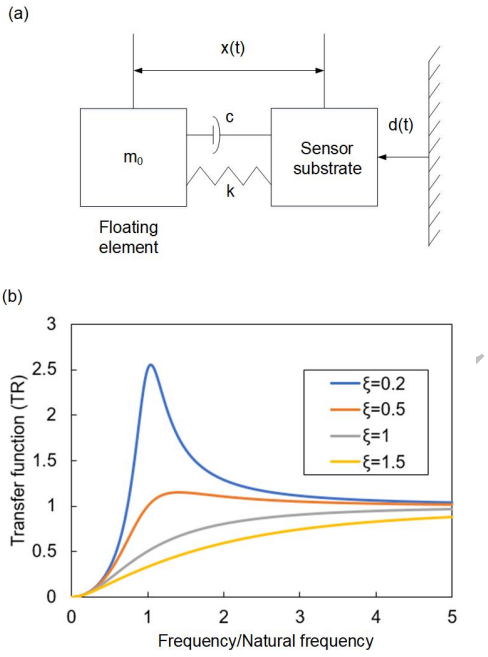

Fig. 2 Mechanical dynamic characteristics of the shear sensor. **a** Simplified model of the floating element suspended by a set of flexure beams fixed to the sensor substrate, which is subjected to outside vibrations. **b** Dynamic response of the optical encoder attached to the sensor substrate, which vibrates at different frequencies.

dimensions were built and simulated with Comsol 4.0 as shown in Fig. 3. The two anchors of the beams were fixed while the rest of the surfaces was freed in the model. As shown in Figs. 3a-c, spring constants were simulated by applying the same load from three directions (spanwise direction F_x, streamwise direction F_y and vertical-to-shear-plane direction F_z) to compare the sensitivity of the flexural beams in various directions. Figs. 3a-c show the FEA results for one exemplary floating element with 18.6 mN of load applied in all three directions. The folded beams were assumed to be 0.5 mm wide, 6 mm thick, and 50 mm long. As a result, the floating element displaced ~1.95 µm in the streamwise direction, while shifting only ~0.05 µm in the spanwise direction and ~0.07 µm in vertical-to-shear-plane direction. This indicates the folded beams are much stiffer in the spanwise and vertical-to-shear-plane direction than the streamwise direction. Fig. 3d shows the maximum stress inside the beams at maximum displacement due to the aforementioned load. The stress value, 3.75 MPa, is only 1-2% of the yield stress of the aluminum 6061 alloy (~250 MPa) used for the main plate of the shear sensor in this study.

The resonant frequencies and associated modes for

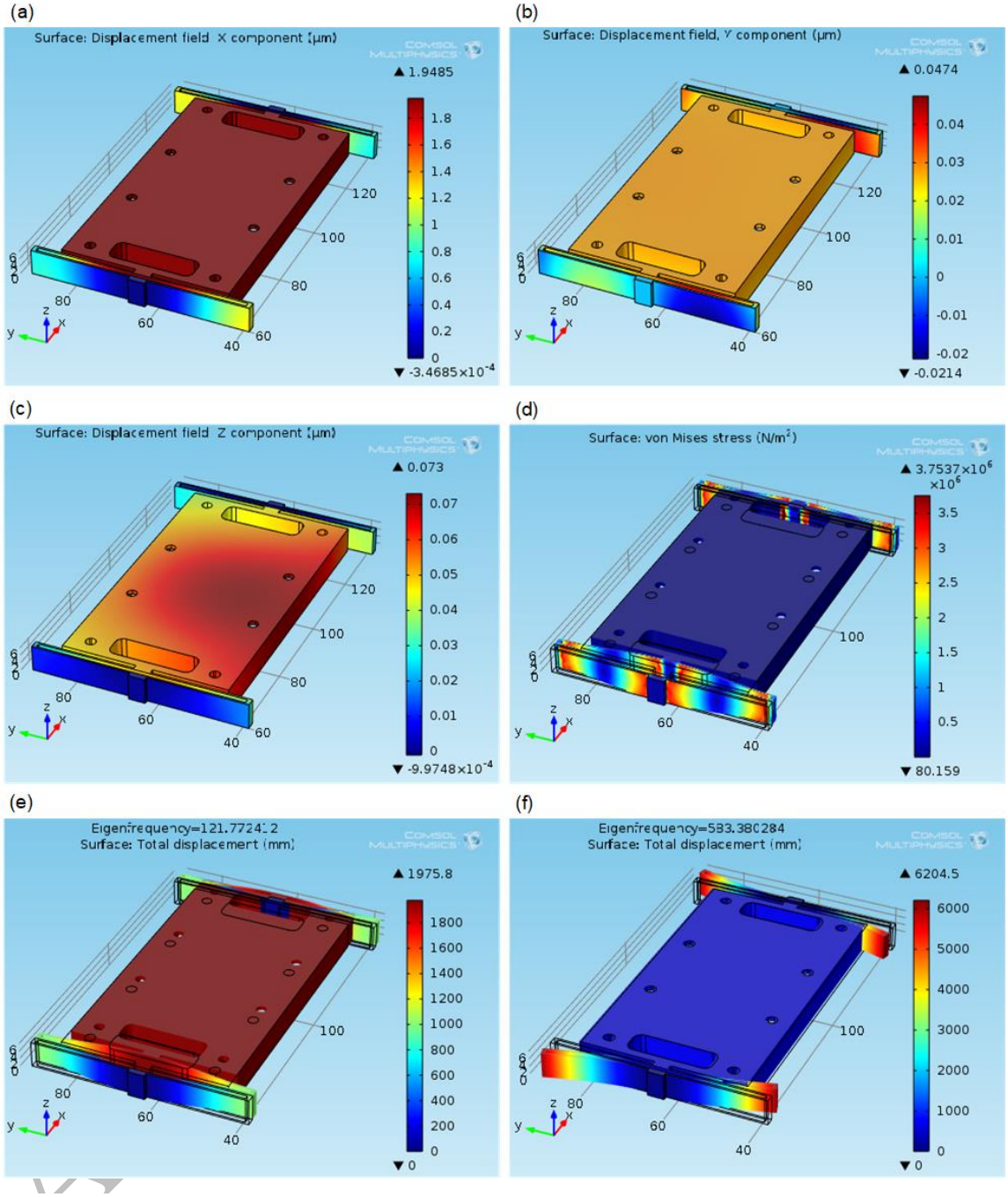

Fig. 3 FEA analysis of the floating element. **a** Displacement of the floating element in streamwise direction. **b** Displacement of the floating element in transverse direction. **c** Displacement of floating element in vertical-to-shear-plane direction. **d** Shear stress distribution. **e** First mode of resonance with eigenfrequency. **f** Second mode of resonance with eigenfrequency.

the floating element were also studied in FEA. Figs. 3e-f show the first two mode shapes together with the resonant frequencies. As can be seen in the figures, the lowest resonant frequency for vibration along the streamwise direction is ~120 Hz, close to the value calculated using basic beam theory (~124 Hz). This value is higher than the environmental noises (< 60 Hz) that we commonly encountered in various flow facilities. With the "low-pass" behavior of the system, the shear sensor is not influenced by these common

environment noises.

3 Sensor fabrication

3.1 Machining of the floating element

Fabrication of highly flexible folded beams that can suspend a large (i.e., larger than a few centimeters) floating element has been the main bottleneck against adopting the MEMS-type configuration for regular scale shear sensors. To overcome the size and material limitations of the shear sensors currently obtainable by MEMS fabrication technologies, i.e., a few centimeters and made of silicon (Shajii 1992; Sheplak 2004; Sun 2015), the following approach has been taken. To obtain the friction drag of sample surfaces larger than ~5 cm in length and width (Lee 2016) for a macroscale object in motion, one would need a shear sensor made of metal with a floating element larger than ~5 cm in length and width. Here, the metal beams and floating elements were monolithically machined from one metal plate. Wire-EDM was chosen due to its excellent machining precision, ability to make high-aspect-ratio beam structures, and potential for mass manufacturing. However, using wire-EDM to naively machine the extremely flexible beams needed for the current shear sensor was not possible, especially with a large and heavy floating elements attached to and suspended by the beams. None of the professional EDM companies that we placed orders with were able to obtain the required structures. When cutting the highly flexible folded beam (e.g., 110 mm long, 6 mm thick and 0.25 mm wide), non-negligible amounts of beam deflection occurred due to thermal stress, dielectric liquid flushing and mechanical vibration. These stresses by disturbances resulted in non-uniform beam widths or even beam breaking, as shown in Fig. 4a.

The above problem was solved by adopting a specially designed path for EDM, as explained in Figs. 4b and 4c. Instead of carving out the flexure beams and floating element using one continuous path, the cutting process was divided into multiple steps, beginning with creating multiple individual slots and then subsequently connecting these individual slots. For step 1 illustrated in Fig. 4b, 12 individual slots were made. Compared with the eventual geometry, the unremoved portions may be viewed as having temporary connections, which serve to keep the eventual beams and floating element attached to the main plate throughout the cutting operations of step 1. Because the temporary connections formed between the individual slots are short and not flexible, they were obtained with a uniform width and gap size. After step 1 was completed, step 2 removed the 4 temporary connections shown with blue lines to connect 4 pairs of slots, thus obtaining 4 folded beams. Because these connecting cuts were short and at the ends of the beams, there was no risk of breaking the beams. In step 3, the large floating element was released by removing the 4 temporary connections shown with red lines at the 4 corners, completing the machining process of the main plate.

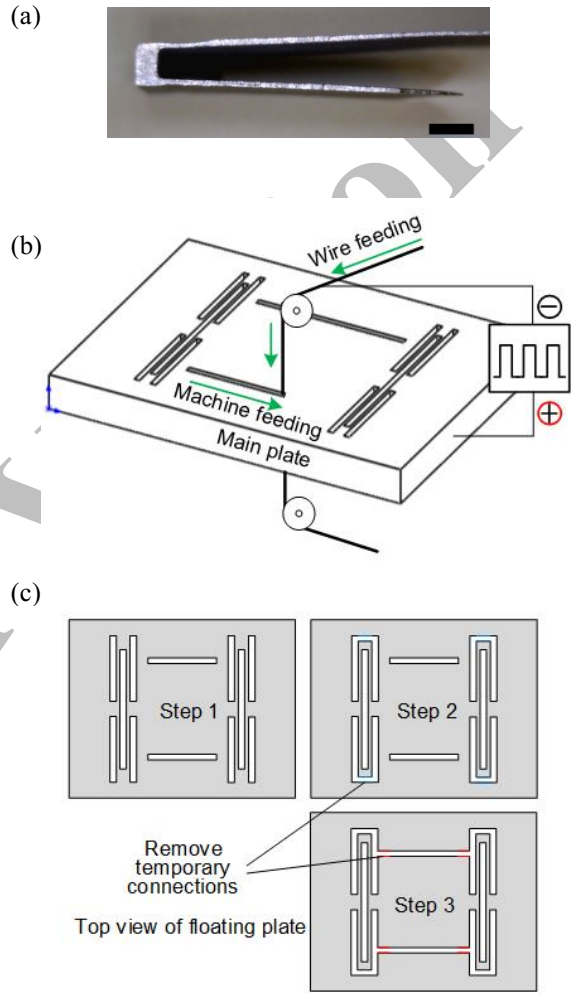

Fig. 4 Machining of a floating element suspended by a set of flexure beams, which are highly flexible in one direction but rigid in all other directions, within the main plate made of a single piece of metal (drawn for one of the two floating elements machined in one plate). **a** A broken beam commonly found when regular wire-EDM practice was naively used, viewed from above the plate. The black scale bar is 3 mm. **b** Schematic illustration of EDM process completing step 1. **c** The EDM path was divided into multiple isolated segments (3 steps shown) to successfully fabricate the extremely flexible beams that suspend the floating element for the current shear sensor.

3.2 Strategy for reduced machining cost

To lower machining cost, multiple plates can be stacked on top of one another and machined simultaneously by the wire-EDM to reduce the manufacturing time and cost per plate (Arihara 2019) as demonstrated in Fig. 5. Similar to the single plate machining process, groups of slots must be cut in a specific order, as mentioned previously. However, unlike a single plate, for which the wire EDM process could be completed by removing the slugs after each slot is cut, for a stack of multiple plates it was difficult to remove the multiple slugs formed within the thick stack. To overcome this difficulty, a pocketing strategy was adopted instead, which eroded away all the material within the slots by gradually spiraling outwards from the centerline of each slot by a certain stepover value. While this increased the cutting time by roughly 1.5 times, it was a necessity for machining a thick stack of multiple plates, as detailed in (Arihara 2019).

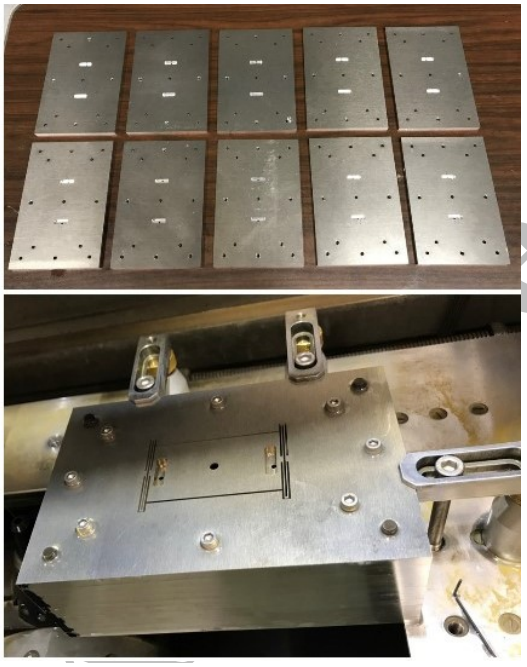

Fig. 5 Ten plates machined simultaneously by processing a stack of ten aluminum plates with wire-EDM.

As shown in Fig. 5, a stack of ten plates were machined successfully using this modified wire-EDM process. The floating element and flexure beams on each of the finished plates was confirmed to have the same geometric values as that of the individually machined plate, confirming the effectiveness of simultaneously machining multiple plates at once for increased throughput and lowered cost.

3.3 Sensor assembly

Figure 6 explains the assembly process for the shear sensor using cross-sectional views. In Fig. 6a, the cover sheet (shown in gray) was first installed onto the main plate and fixed by a set of screws (shown in red) from the back of the plate. In Fig. 6b, the sample surface (shown in pink) was then installed onto the floating element by inserting a set of screws (shown in red) from the backside of the floating element. A feeler gauge was used to ensure a proper gap distance between the trailing edge of the sample surface and the edge of the cover sheet. Note the optical scale (shown in green) attached on the bottom surface of the floating element. Finally, as shown in Fig. 6c, the encoder plate was attached to the main plate via a set of screws (shown in red). An optical encoder was located inside a cavity formed within the encoder plate and covered with a glass window (shown in light gray) that has been sealed to be waterproof. The alignment of the encoder relative to the optical scale was crucial to the functioning of the encoder. This proper alignment was achieved through proper tolerancing during the design process, careful machining of the sensor, and use of the encoder's built-in alignment indicator.

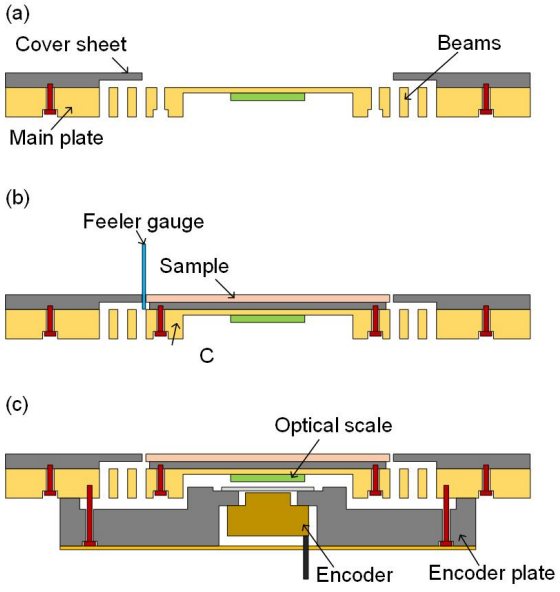

Fig. 6 Mechanical assembly of the shear sensor. **a** Install a cover sheet onto a main plate. **b** Install two sample surfaces onto the two floating elements in the main plate using feeler gauges for alignment and spacing with the cover sheet. **c** Assemble the encoder plate, which houses two encoders (one per floating element), onto the main plate. All assembly steps use screws, avoiding glue, to support repetitions of sample mounting and dismounting for repeated experiments.

4 Sensor characterization

4.1 Optical encoder alignment and calibration

The optical encoder is used to measure the displacement of the floating element with high accuracy. The encoder works by emitting a laser beam onto the gratings of the optical scale and detecting the reflected interference patterns, which is known as Talbot effect (Mitchell 2008). The accuracy of the encoder is very sensitive to the distance between the encoder head (optical detector) and optical scale (which displaces with the floating element). For the linear encoder used in this sensor system (M2000 linear encoder, Celera Motion Inc.), the product manual gives the optimal distance for usage in air to be 2.4±0.15 mm. However, the provided value cannot be applied directly if the sensor is used underwater where the emitted light from the encoder passes through 2 media with different refractive indices – water and the encoder window. Difficulty in precisely calculating the appropriate distance led us to perform a calibration study to quantify the optimal distance for underwater usage.

As shown in Fig. 7, spacers of different thicknesses were used during the calibration process to control the distance between the encoder and the optical scale. First, the scale plate was placed on the worktable and adjusted to be horizontal. Then, the encoder head was installed onto the encoder, along with the junction plate. Two metal spacers were placed between encoder plate and scale plate to ensure the encoder head is parallel to the optical scale and that the encoder head and optical scale are aligned in the XY directions, per the encoder's specifications. After this alignment process, the junction plate was fixed onto the upper plate of the worktable with glue. Then, the scale plate was moved up towards the encoder in 10 µm increments until the optimal Z-distance was found. With the above method, a Z-distance of 2.68±0.46 mm was found to produce the strongest signal intensity on the encoder under water and thus selected as the optimal optical distance for underwater applications.

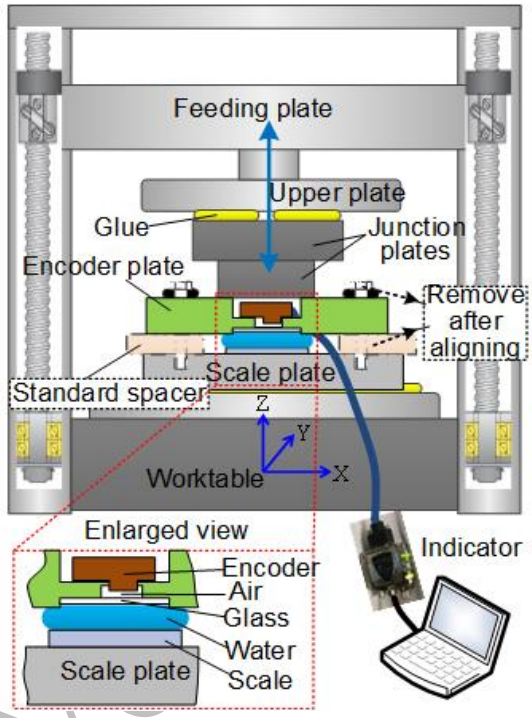

Fig. 7 Calibration of the optical encoder for underwater application.

4.2. Spring constant and resonant frequency

The spring constants of the flexure beams were measured by applying gravity to the streamwise direction. The floating elements were positioned vertically using a level and incrementally displaced by hanging different weights of known mass, as shown in Fig 8. The displacement signals from the encoders were recorded and post-processed. The measured displacements, corresponding to the different weights, exhibited a strong linear correlation, confirming the expected mechanical response. The flexure beams of two floating elements were found to have slightly different spring constants due to the minute variations

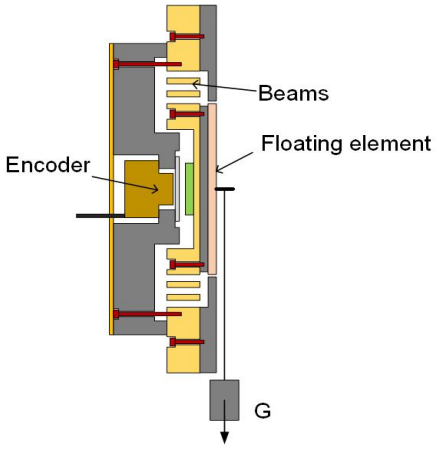

Fig. 8 Measurement of spring constant of the flexure beams for each floating element.

in the wire-EDM process, indicating the need to compensate for the difference when comparing displacement values from the two floating elements. Resonant frequency was also measured using a step load process. A pulse load was applied to the floating element, which was allowed to be damped by air. Using a fast Fourier transform, the resonant frequency was found to be ~118 Hz, which is close to the 120 Hz predicated by FEA.

4.3 Sensor utility assessment

Designed to be low-profile and capable of being used in different flow facilities, the shear sensor has been tested successfully in a water tunnel, wind tunnel, and under a boat. The main purpose was to demonstrate its versatility by confirming the developed sensor can be installed with a relative ease and produce reasonable data for all three cases rather than fully characterizing its performance in this first report. As shown in Fig. 9a, the shear sensor was used in a small water tunnel to measure the shear stress on both smooth and SHPo surfaces in turbulent boundary layer (TBL) flows. The results summarized in Fig. 9c confirmed that the skin friction on a SHPo surface was lower than that of a smooth surface. However, this water tunnel was too small to fit a regular sensor with two floating elements. Instead, a smaller sensor with only one floating element was used, and SHPo and smooth surfaces were measured separately and compared after the tests. The shear sensor was also used in a small wind tunnel to measure the friction drag ratio between a smooth surface and a riblet surface simultaneously, as shown in Fig. 9b. The riblet surface was fabricated from silicon using MEMS fabrication technology to duplicate the riblet geometry that produced the largest drag reduction in Dean and Bhushan (2010). The obtained results in Fig. 9d matched their published results, confirming the utility of the current shear sensor for wind tunnel experiments as well. The shear sensor was further used in harsh flow conditions to measure the friction drag ratio between a smooth surface and a SHPo surface simultaneously. Mounted at the bottom of the boat, as shown in Fig. 10, and tested in open water at Reynolds numbers of up to $6x10^6$ (speeds of up to 6 m/s), the sensor showed reliable performance even under harsh flow conditions, being able to accurately measure the drag reduction of SHPo surfaces. The detailed results of the boat tests are being presented elsewhere.

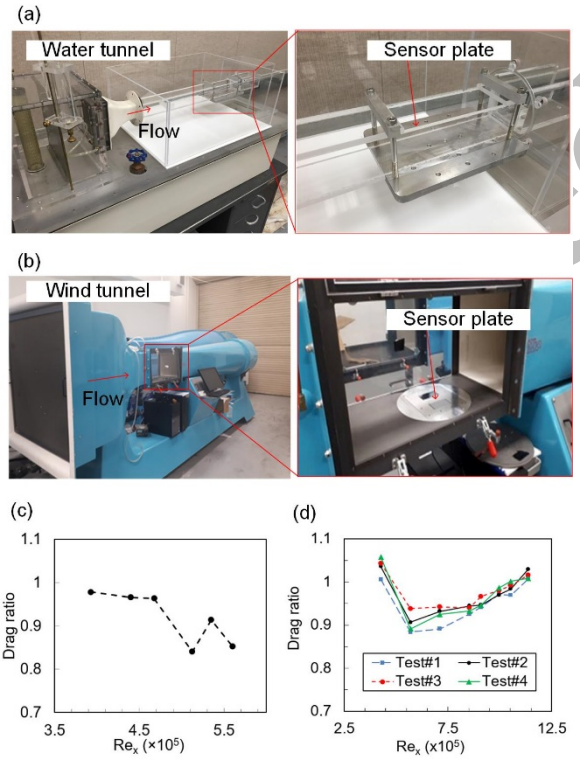

Fig. 9 Use of the shear sensor in both water tunnel and wind tunnel. **a** Tested in water tunnel. **b** Tested in wind tunnel. **c** Drag ratio of a SHPo surface to the smooth surface tested in water tunnel over a range of Reynolds numbers. **d** Drag ratio of a riblet surface to the smooth surface tested in wind tunnel over a range of Reynolds numbers.

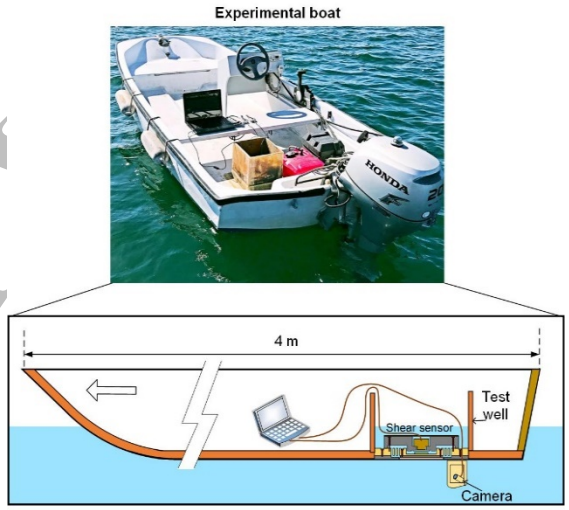

Fig. 10 Use of the shear sensor under a motorboat in open water. The sensor replaced a portion of the hull. Note an underwater camera attached at immediate downstream of the shear sensor to monitor the sample surface.

4.4 Uncertainty analysis

Although the reported sensor is best utilized as a shear comparator between two different surface samples placed on two floating elements, each floating element can be used as an own shear sensor if properly calibrated. Uncertainty analysis has been carried out to estimate the level of confidence on the measured shear force F on a floating element for the full utility. Four major sources of errors are identified and analyzed below.

The first error source is the height misalignment between the surface of the sample attached on the floating element and the surface of the cover sheet

surrounding the floating element; see Figs. 1b and 6. This height misalignment is usually considered the single largest source of error for floating-element-based shear sensors (Schetz 2010; Allen 1976; Allen 1977; Winter 1979; Haritonidis 1989). A significant effort was undertaken to ensure the sample surfaces were flush with or slightly lower than the surrounding cover sheet surfaces. During the assembly process shown in Fig. 6, a portable microscope (Depth Measuring Portable Microscope, GWJ Co.) was used to ensure the height step is between 0 and 5 μm, i.e., smaller than 5 wall units (or the viscous sublayer thickness) for the low Mach number flows exemplified in Fig. 9. Accordingly, the bias error b_1 is negative with the magnitude smaller than 5%, based on previous studies (Haritonidis 1989; Smith and Walker 1958; MacLean and Schetz 2003).

The second error source is the horizontal gaps between the floating element and the surrounding cover sheet. Feeler gauges (Dwyer, ~50 μm) were used to obtain uniform horizontal gaps of desired values. The horizontal gap was designed to be ~0.01% of the streamwise dimension of the floating element and implemented to be so by machining the cover sheet accordingly. For low Mach number applications with $Re_x < 10^7$ as exemplified in Fig. 9, the horizontal gap size was about 50 wall units, resulting in bias error b_2 smaller than 5%, based on previous studies (MacLean and Schetz 2003).

The third error source comes from the resolution of the optical encoder. Since the resolution of the encoder used for the tests in Fig. 9 was 78 nm, the random error s_3 for the utility assessment was 78 nm. The fourth error source comes from the spring constant measurement shown in Fig. 8. With ±1° angle variation between the floating plate displacement direction and the gravity direction, the bias error b_3 was ±0.02%. As the same encoder was used, its resolution also generated random error s_4. Besides the four error sources mentioned above, other error sources were found negligible, including misalignment between flow direction and sensor defection direction, encoder self-heating, span shift, zero shift, and hysteresis.

The measured shear force F is the product of two independent measurements: spring constant k and floating element displacement D. The bias and random error for F can be estimated by combining errors in these two measurements through a Taylor series expansion:

$$b_F = \sqrt{(\frac{\partial F}{\partial k} b_k)^2 + (\frac{\partial F}{\partial D} b_D)^2} \quad (4)$$

$$s_F = \sqrt{(\frac{\partial F}{\partial k} s_k)^2 + (\frac{\partial F}{\partial D} s_D)^2} \quad (5)$$

where b_F, b_k, and b_D are the bias errors and s_F, s_k, and s_D are the random errors for F, k, and D, all respectively. Assuming the four major error sources above are independent, the total bias or random error for spring constant or displacement are:

$$+b_D = b_2 = 0.05D[m], -b_D = b_1 = 0.05D[m] \quad (6)$$

$$b_k = b_4 = 0.0002k\ [N/m] \quad (7)$$

$$s_D = s_3 = 7.8\times10^{-8}\ [m] \quad (8)$$

$$s_k = s_4 = 7.8\times10^{-8} k / D\ [N/m] \quad (9)$$

By combining Eqs. 4-9 and ignoring insignificant terms, the bias error b_F was calculated to be 5% of the measured shear force F and the random error was calculated to be $s_F = 1.1\times10^{-7}k$. With the given encoder and the low Mach number flow application exemplified in Fig. 9, the shear sensor spring constant k was designed to have the random error s_F within 1% of the measured shear force F. If a smaller spring constant is needed for applications with smaller shear force but cannot be obtained due to manufacturing limit, encoders with a higher resolution may be used to reduce the random error. Following Coleman et al. (1999), the total uncertainty (with a 95% confidence) in measured shear force F is found as:

$$U_F = 2(b_F^2 + s_F^2)^{1/2} = 0.1F \quad (10)$$

This uncertainty is about 10% of the measured shear force.

Since the reported sensor was developed mainly to measure the relative drag ratios (e.g., drag reduction of SHPo surface compared to smooth surface) between two samples accurately under varying and uncontrollable flow conditions, the validity was tested by measuring the shear stress on two identical smooth surfaces attached to two floating plates, as summarized in Fig. 11. For the calibration in the water tunnel, where simultaneous measurement of two surfaces was not possible, the skin friction coefficients was measured on a smooth surface and found matching the empirical value for TBL flows (Schlichting 1987), as shown in Fig. 11a. For the calibration in wind tunnel and with the boat test, the shear forces measured simultaneously on two smooth surfaces on the two floating elements were found nearly identical, as shown in Figs. 11b and 11c, respectively. For the above calibration tests under three different flow settings, the variations were found to be less than 7%.

5 Miniature underwater camera system

To observe the behavior of the SHPo surface during testing, a minimally-intrusive miniature underwater camera system was designed and fabricated, as shown in Fig. 12. This system was comprised of two Ehome waterproof endoscopes and a 3D printed housing unit

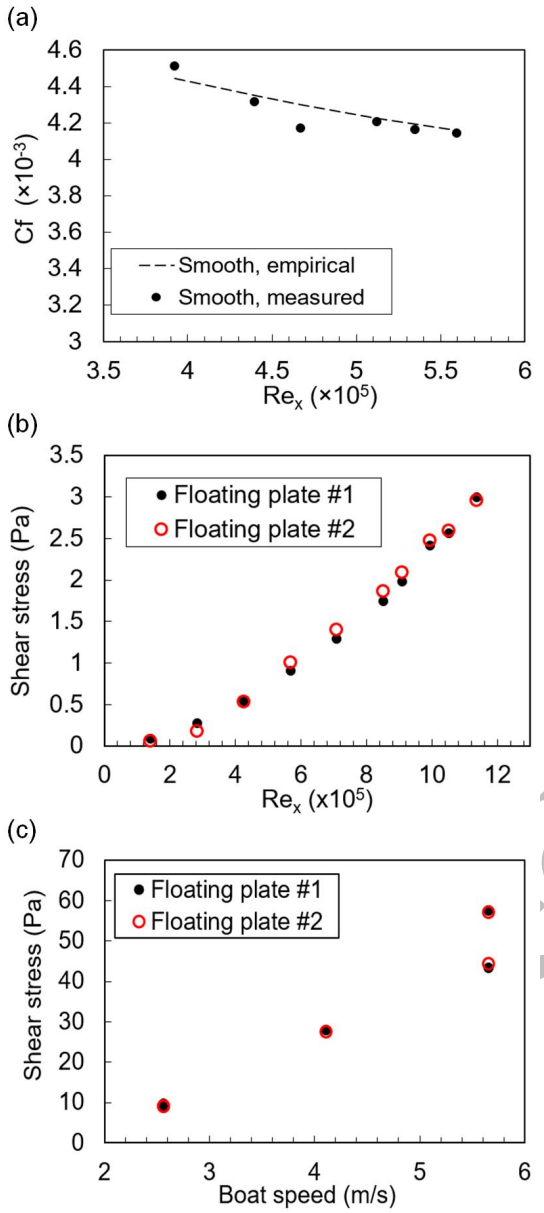

Fig. 11 Calibration by measuring shear stress on only smooth surfaces over a range of flow speeds. **a** Calibration in water tunnel. Skin friction coefficients were measured on a smooth surface and found matching a theoretical (empirical) curve (Schlichting 1987). **b,c** Calibration in wind tunnel and boat test, respectively. Drags of two smooth surfaces were measured simultaneously and found nearly identical. Flow speed was given for the boat test, whose dynamic conditions made it difficult to obtain Reynolds numbers.

to hold the cameras in place. The external geometry of the housing unit was defined by a 4-digit NACA aerofoil equation that would allow for fluid flow to glide across the surface of the housing without creating a boundary layer that would disturb the SHPo surface. Fig. 12a shows a semi-transparent view of the camera housing system, where it can be seen that the two parallel cameras are directed downwards towards the SHPo surface at an angle of 20° from the horizontal plane. This angle value was determined by accompanying research (Yu and Kim 2018). Two cameras are used instead of one so that the upstream and downstream halves of the SHPo surface lay within the focal range of each respective camera. Fig. 11b shows the images of the upstream and downstream halves of the sample surface captured by this camera system.

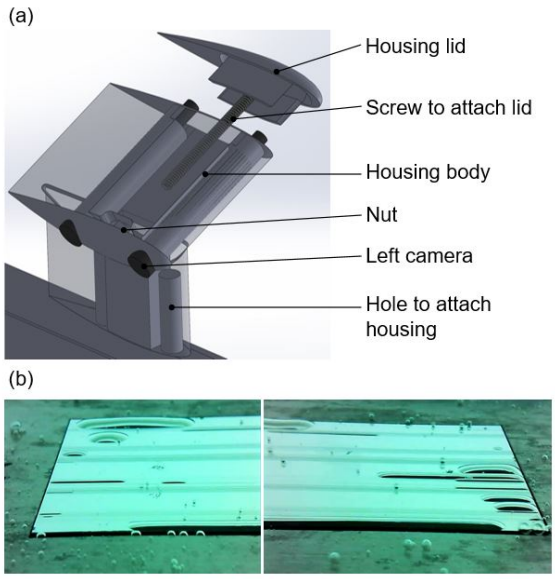

Fig. 12 Miniature underwater camera system. a CAD model of camera housing and two endoscope cameras inside the housing. **b** Resulting images of the upstream (left) and downstream (right) half of the sample surface.

6. Conclusions

We have developed a shear-sensing system to directly compare the friction drag on two different surfaces in both liquid and gas flows. This high-accuracy sensor system was designed to be low-profile for ease of integration into different flow facilities, including water tunnel, towing tank, watercraft, wind tunnel and aircraft. Due to its monolithic construction from a single metal plate and high thickness-to-width aspect ratio beams, the floating elements of the sensor were robust enough to mount and dismount surface samples and allow for reliable measurements under harsh flow and environmental conditions. Dividing the cutting

process into multiple isolated paths enabled the use of wire-EDM to achieve flexure beams that are extremely flexible in the flow direction but rigid in all others. The developed system has been demonstrated to function well at different flow facilities, showing a potential to become a common shear sensor for a range of hydrodynamic and aerodynamic applications.

Acknowledgements

This work was supported by DARPA HR0011-15-2-0021 and NSF 1336966 as well as Volgenau Endowed Chair in Engineering (C.-J.K.). Editing by Danning Yu is appreciated.

References

Aljallis E, Sarshar MA, Datla R, Sikka V, Jones A, Choi CH (2013) Experimental study of skin friction drag reduction on superhydrophobic flat plates in high Reynolds number boundary layer flow. Phys Fluids 25:025103

Allen JM (1976) Systematic study of error sources in supersonic skin-friction balance measurements.

Allen JM (1977) Experimental study of error sources in skin-friction balance measurements. Journal of Fluids Engineering 99:197-204

Arihara B (2019) Manufacturing of Dual Shear Sensing System and Implementation to Boat and Wind Tunnel. MS Thesis, University of California, Los Angeles (UCLA)

Bidkar RA, Leblanc L, Kulkarni AJ, Bahadur V, Ceccio SL, Perlin M (2014) Skin-friction drag reduction in the turbulent regime using random-textured hydrophobic surfaces. Phys Fluids 26:085108

Chandrasekharan V, Sells J, Meloy J, Arnold DP, Sheplak M (2011) A Microscale Differential Capacitive Direct Wall-Shear-Stress Sensor. Journal of Microelectromechanical Systems 20:622-635

Choi C-H, Kim C-J (2006) Large slip of aqueous liquid flow over a nanoengineered superhydrophobic surface. Phys Rev Lett 96:066001

Coleman HW, Steele Jr WG, Steele WG (1999) Experimentation and uncertainty analysis for engineers. John Wiley & Sons,

Dean B, Bhushan B (2010) Shark-skin surfaces for fluid-drag reduction in turbulent flow: a review. Philosophical Transactions of the Royal Society A: Mathematical, Physical and Engineering Sciences 368:4775-4806

Haritonidis JH (1989) The measurement of wall shear stress Advances in fluid mechanics measurements. Springer, pp. 229-261

Ho C-M, Tai Y-C (1998) Micro-electro-mechanical-systems (MEMS) and fluid flows. Annu Rev Fluid Mech 30:579-612

Jung YC, Bhushan B (2010) Biomimetic structures for fluid drag reduction in laminar and turbulent flows. J Phys: Condens Matter 22:035104

Lee C, Choi C-H, Kim C-J (2008) Structured surfaces for a giant liquid slip. Phys Rev Lett 101:64501

Lee C, Choi C-H, Kim C-J (2016) Superhydrophobic drag reduction in laminar flows: a critical review. Exp Fluids 57:176

MacLean M, Schetz JA (2003) Numerical study of detailed flow affecting a direct measuring skin-friction gauge. AIAA Journal 41:1271-1281

Meritt RJ, Schetz JA (2014) Skin Friction Sensor Validation for High-Speed, High-Enthalpy Flow Applications. AIAA 2014 2800

Mitchell DK (2008) A radiation-hardened, high-resolution optical encoder for use in aerospace applications. In: Proceedings of the 2008 IEEE Aerospace Conference. IEEE, Big Sky, Montana, pp 1-7

Natarajan V, Kathiresan M, Thomas K et al. (2014) MEMS Sensors for Underwater Applications Micro and Smart Devices and Systems. Springer, pp. 487-502

Naughton JW, Sheplak M (2002) Modern developments in shear-stress measurement. Progress in Aerospace Sciences 38:515-570

Rothstein JP (2010) Slip on superhydrophobic surfaces. Annu Rev Fluid Mech 42:89-109

Schetz JA (2010) Direct measurement of skin friction in complex flows. Paper No AIAA 44

Schlichting H (1987) Boundary-layer theory. McGraw-Hill,

Shajii J, Ng K-Y, Schmidt MA (1992) A microfabricated floating-element shear stress sensor using wafer-bonding technology. Journal of Microelectromechanical Systems 1:89-94

Sheplak M, Cattafesta L, Nishida T, McGinley CB (2004) MEMS shear stress sensors: promise and progress. Defense Technical Information Center,

Smith DW, Walker JH (1958) Skin-friction measurements in incompressible flow. National Advisory Committee for Aeronautics,

Sun G, Park H, Kim C-J (2015) Development of a Miniature Shear Sensor for Direct Comparison of Skin-Friction Drags. Journal of Microelectromechanical Systems 24:1426-1435

Winter K (1979) An outline of the techniques available

for the measurement of skin friction in turbulent boundary layers. Progress in aerospace sciences 18:1-57

Xu M (2017) Design, fabrication, and evaluation of superhydrophobic (SHPo) surfaces for drag reduction in turbulent boundary layer fows. Ph.D. Dissertation, University of California, Los Angeles (UCLA)

Yu N, Kim C-J (2018) Detecting the sub-states of grating superhydrophobic surfaces with naked eyes. In: Proceedings of the 2018 IEEE Micro Electro Mechanical Systems (MEMS). IEEE, pp 1293-1295

Zhang X, Armstrong WD, Lindberg WR, Naughton JW (2012) Experimental validation of a dynamic resonant wall shear stress sensor. Exp Fluids 53:1107-1121

Zhang X, Naughton J, Lindberg W (2008) Working Principle Simulations of a Dynamic ResonantWall Shear Stress Sensor Concept. Sensors 8:2707-2721